Type-I and type-II Weyl fermions, topological depletion, and universal subleading scaling across topological phase transitions

Fadi Sun and Jinwu Ye

Department of Physics, Capital Normal University, Key Laboratory of Terahertz Optoelectronics, Ministry of Education, and Beijing Advanced Innovation Center for Imaging Technology, Beijing 100048, China

Department of Physics and Astronomy, Mississippi State University, P.O. Box 5167, Mississippi State, Mississippi 39762, USA and Kavli Institute of Theoretical Physics, University of California, Santa Barbara, California 93106, USA

(Received 20 January 2017; published 7 July 2017)

It is well established that physical quantities satisfy scaling functions across a quantum phase transition with an order parameter. It remains an open problem if there are scaling functions across a topological quantum phase transition (TQPT) with extended Fermi surfaces (FSs). Here, we study a simple system of fermions hopping in a cubic lattice subject to Weyl-type spin-orbit coupling (SOC). As one tunes the SOC parameter at half filling, the system displays both type-I and type-II Weyl fermions and also various TQPTs driven by the collision of particle-particle or hole-hole Weyl FSs. At zero temperature, the TQPT is found to be third order, and its critical exponents are determined. Then we investigate if the physical quantities such as specific heat, compressibility, and magnetic susceptibilities satisfy any sort of scaling across the TQPT. In contrast to all the previous cases in quantum or topological transitions, we find that although the leading terms are nonuniversal and cutoff dependent, the subleading terms are nonanalytic and satisfy universal scaling relations. The subleading scaling leads to topological depletions which show non-Fermi-liquid corrections and $\sqrt{T}$ quantum cusps. One can also form a topological Wilson ratio from the subleading scalings of two conserved quantities such as the specific heat and the compressibility. One may also interpret the type-I and type-II Weyl fermions as a TQPT driven by the collision of particle-hole Weyl FSs. Experimental realizations and detections in cold-atom systems and materials with SOC are discussed.

DOI: 10.1103/PhysRevB.96.035113

I. INTRODUCTION

Quantum phase transitions with an order parameter have been under intense investigations since the experimental discovery of high-temperature superconductivity. It is known that various experimental measurable physical quantities near a quantum phase transition satisfy various universal scaling functions at a finite temperature [1,2]. On another front, topological phases and phase transitions without an order parameter have also been explored since the experimental observations of the quantum Hall effects [3]. Topological phenomena in various fermionic systems [4,5] have come back into focus since the more recent experimental realizations of a new kind of insulator called topological insulators [6,7]. It is natural to study scaling functions across various topological phase transitions without an order parameter. There have been previous efforts to derive leading scaling functions across a topological quantum phase transition (TQPT) such as the quantum Hall to insulator transition in [8,9] and that driven by collisions of Dirac points in a honeycomb lattice [10]. All these TQPTs can be scaled to a single point in momentum space, so the conventional renormalization group (RG), large-N expansion, and other methods can be applied to capture low-energy critical fluctuations and derive the scaling functions.

Here, we study a simple system in which free fermions hop in a cubic lattice subject to a Weyl type of spin-orbit coupling [11]. There are experimental motivations of this model from both cold atoms and materials, which will be discussed in Sec. VII. As one tunes the spin-orbit-coupling (SOC) parameters at half filling, the system displays both type-I and type-II fermions and also various TQPTs driven by the collision of extended particle-particle or hole-hole Weyl Fermi surfaces (FSs). The previous RG analysis scaled to a single Dirac point in momentum space in [8–10] does not apply to such a situation due to the low-energy excitations around the extended FS. Unfortunately, the previous RG analysis [12,13] designed to deal with leading scalings around a closed and extended FS do not apply here either due to various cone singularities of the FS geometry at the TQPT. Intuitively, we do not expect the physical quantities such as specific heat, compressibility, and magnetic susceptibilities to satisfy any leading scalings across the TQPT. However, it is important and interesting to investigate if they satisfy any sort of scaling different from the leading scalings. At zero temperature, the TQPT is found to be a third-order one whose critical exponent is determined. Then we find that in contrast to all the previous cases in quantum and topological transitions, although the leading terms in all these physical quantities are nonuniversal and cutoff dependent, the subleading terms satisfy universal scaling relations. This fact is a unique and salient feature of this kind of TQPT with extended FS reconstructions. The subleading scaling leads to the topological depletions (TDs) which show non-Fermi-liquid corrections and $\sqrt{T}$ quantum cusps. The TDs show nonanalytic behaviors in the quantum critical regime which can be easily distinguished from the analytic leading terms and detected experimentally. One can also form a topological Wilson ratio from the subleading scalings of two conserved quantities such as the specific heat and the compressibility. One may also interpret the type-I and type-II Weyl fermions as a TQPT driven by collision of particle-hole Weyl FSs. We provide an intuitive classification scheme for the TQPT in terms of the collisions of FSs in the particle-hole and particle-particle (or hole-hole) channels, augmented by

the associated leading or subleading scaling functions. Some possible connections with the subleading topological entanglement entropy and classical cusps in the $O(3)$ Heisenberg model are briefly discussed. Some possible perspectives are outlined. Experimental realizations and detection in cold-atom systems and materials with SOC are discussed.

II. TYPE-I WEYL FERMIONS AS A TQPT

The Hamiltonian of fermions hopping in a cubic lattice subject to Weyl-type spin-orbit coupling in Fig. 1(a) can be written as

$$H = \sum_k h_i(\boldsymbol{k})\sigma_i, \quad i = 0,x,y,z, \tag{1}$$

where σ_0 is the identity matrix, $\sigma_{x,y,z}$ are three Pauli matrices, and $h_0(k) = -2t(\cos\alpha\cos k_x + \cos\beta\cos k_y + \cos\gamma\cos k_z)$, $h_x(k) = 2t\sin\alpha\sin k_x$, $h_y(k) = 2t\sin\beta\sin k_y$, $h_z(k) = 2t\sin\gamma\sin k_z$. The non-Abelian gauge parameters (α,β,γ) are shown in Fig. 1(b). The Hamiltonian's two energy bands are $\epsilon_\pm(k) = h_0(k) \pm h(k)$, where $h(k) = \sqrt{[h_x(k)]^2 + [h_y(k)]^2 + [h_z(k)]^2}$. Since t is the only energy scale, we choose $2t = 1$ for later calculations. At half filling $\mu = 0$, the particle and hole FS is given by

$$\epsilon_\pm(k) = 0. \tag{2}$$

It is easy to see that the particle energy is related to that of the hole $\epsilon_+(\vec{k} + \vec{Q}) = -\epsilon_-(\vec{k})$, where $\vec{Q} = (\pi,\pi,\pi)$ is the FS nesting vector which separates the particle FS from the hole FS. It is this separation which distinguishes the TQPT in a particle-particle or hole-hole FS from that of type-I Weyl fermions in Fig. 2 and type-II Weyl fermions in Fig. 3, where the particle Weyl Fermi surface (WFS) collides with the hole WFS. It also leads to the relation between the particle density of states (DOS) and that of the hole, $D_+(\omega) = D_-(-\omega)$ at half filling $\mu = 0$.

At the cubic center $(\alpha,\beta,\gamma) = (\pi/2,\pi/2,\pi/2)$ in Fig. 1(b), there are eight type-I Weyl fermions located at $k_x = 0,\pi, k_y = 0,\pi, k_z = 0,\pi$ carrying the topological monopole charges $N_3 = \pm 1$ in Fig. 1(c). The center is the π flux (in all three planes) Abelian point with $\tilde{\tilde{\tilde{SU}}}(2)$ symmetry in the rotated basis. It is the inversion-symmetry breaking in Eq. (1) which leads to their existences. Its dispersion relation $\epsilon^I_\pm(\vec{q}) = \pm\sqrt{q_x^2 + q_y^2 + q_z^2}$ leads to the dynamic exponent $z = 1$ and a vanishing DOS $D(\omega) \sim \omega^2$, so it is a semimetal. Conventional scaling analysis with $z = 1$ in [1,2] leads to $C_v \sim T^3, \chi_u \sim T^2$, which can easily be distinguished from conventional Fermi-liquid (FL) behaviors, $C_v \sim T, \chi_u \sim C$. Here, we focus on rich and interesting topological phase transitions along the three lines emanating from the eight type-I Weyl fermions. We will focus only on the half-filling case $\mu = 0$. Away from the center, some or all Weyl fermions will become closed particle or hole WFSs, as shown in Fig. 2. The WFS still keep the topological monopole charges $N_3 = \pm 1$ of the Weyl fermions [4]. How the WFSs evolve along the three lines $\alpha = \beta = \gamma = \theta; \alpha = \pi/2, \beta = \gamma = \theta$; and $\alpha = \beta = \pi/2, \gamma = \theta$ is shown in Figs. 4, 5, and 6 respectively. The WFSs satisfy $\sum_{i=1}^{8} N_{3i} = 0$ during the evolution. The extension of our

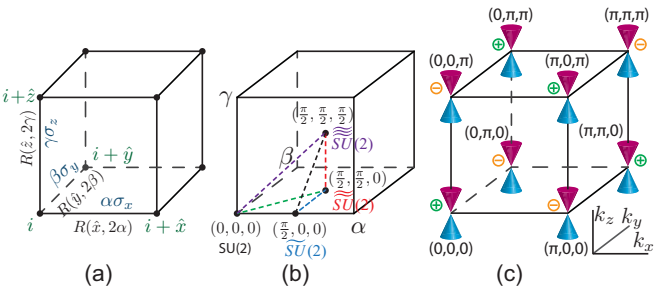

FIG. 1. (a) The non-Abelian gauge fields $(\alpha\sigma_x, \beta\sigma_y, \gamma\sigma_z)$ are put on the three links in a cubic lattice. (b) The (α,β,γ) parameter space. There are one $SU(2)$ Abelian point at the origin and three more Abelian points in the correspondingly rotated frames $\widetilde{SU}(2), \widetilde{\widetilde{SU}}(2), \widetilde{\widetilde{\widetilde{SU}}}(2)$ at the edge, face, and the cubic center, respectively. There are type-I Weyl fermions along the line connecting the cubic center to the edge center and type-II Weyl fermions at the face center. (c) The eight type-I Weyl fermions with the topological charges $N_3 = \pm 1$ at $\alpha = \beta = \gamma = \pi/2$. See Fig. 2 for the Weyl point explanation.

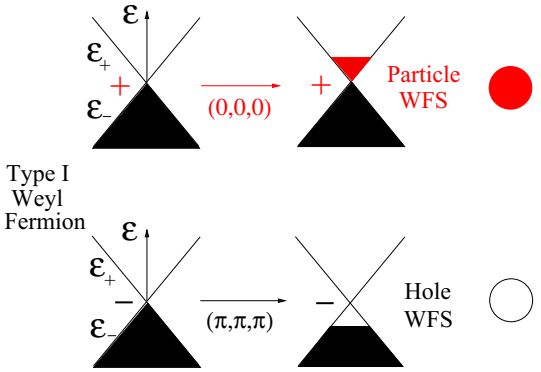

FIG. 2. A pair of type-I Weyl fermions at (0,0,0) and (π,π,π) with opposite topological charges is turned into a particle WFS and a hole WFS, respectively, due to small SOC $\alpha = \beta = \gamma = \theta$. The topological charges are conserved in the process. It is in the $q_z = 0$ cross section with the energy ϵ as the vertical axis. Note the separation between the particle and hole WFS by the FS nesting momentum $\vec{Q} = (\pi,\pi,\pi)$.

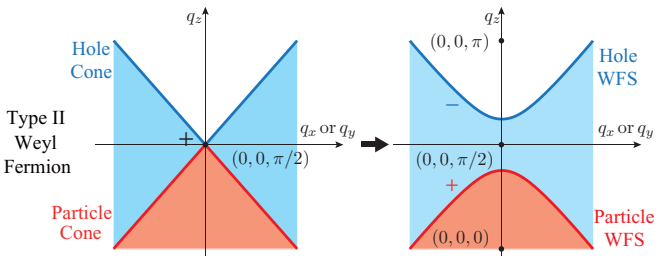

FIG. 3. A type-II Weyl fermion at $(0,0,\pi/2)$ and $\theta_c = 0$ in Fig. 6 can be viewed as a TQPT of a particle WFS and a hole WFS. It is in the cross section of $q_x = 0$ or $q_y = 0$, with q_z being the vertical axis. Under a small SOC $\alpha = \beta = \pi/2, \gamma = \theta$, it splits into a type-I particle WFS with a charge 1 centered at (0,0,0) and a type-I hole WFS with a charge -1 centered at $(0,0,\pi)$.

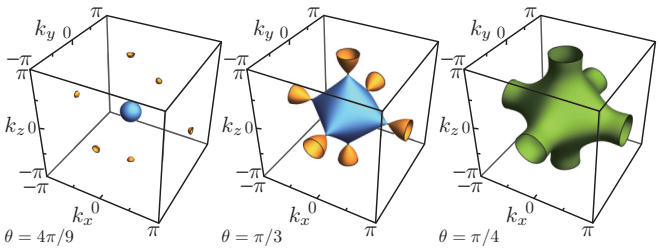

FIG. 4. The particle WFS evolves along $\alpha = \beta = \gamma = \theta$ for $\theta = 4\pi/9, \pi/3, \pi/4$. At the QCP $\theta_c = \pi/3$, the big WFS with $N_3 = 1$ (blue) hits the other three small WFSs (yellow) with $N_3 = -1$ at six Fermi points at $\vec{K}_c = (\pm 2\pi/3, 0, 0), (0, \pm 2\pi/3, 0), (0, 0, \pm 2\pi/3)$. As θ increases further, it becomes a whole (green) Fermi surface with a total $N_3 = 1 - 1 - 1 - 1 = -2$ charge, so it is a topologically nontrivial FS. The hole WFS can be reached by shifting the particle WFS by the FS nesting vector (π, π, π).

analysis to doping cases with $\mu \neq 0$, mapping out the global topological phase diagrams in the chemical potential μ, and the SOC parameter space will be presented in future works.

III. THE THIRD-ORDER TQPT ALONG $\alpha = \beta = \gamma = \theta$ AT ZERO TEMPERATURE

In this section, we focus on the diagonal line $\alpha = \beta = \gamma = \theta$ in Fig. 1(b) and at half filling $\mu = 0$. How the WFS evolves along this line is shown in Fig. 4. Notably, there is a TQPT driven by the collisions of the four WFSs where the colliding four-particle WFS takes a saddle point (cone) geometry near a Von Hove singularity (VHS) $K_c = 2\pi/3$ and the critical SOC parameter $\theta_c = \pi/3$. When expanding around the VHS $K = K_c + \Delta/\sqrt{3}$ and θ_c in Fig. 7, we get the particle energy spectrum:

$$\epsilon_+(\vec{q}) = -\left[\Delta + a q_x^2 - b\left(q_y^2 + q_z^2\right)\right], \tag{3}$$

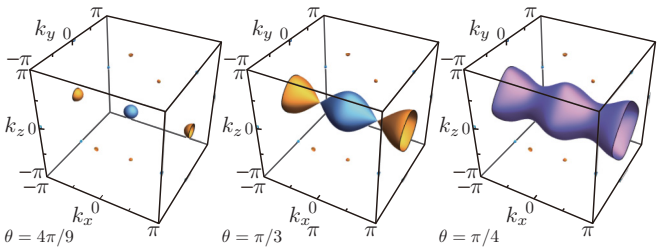

FIG. 5. The particle WFS evolves along $\alpha = \pi/2, \beta = \gamma = \theta$ for $\theta = 4\pi/9, \pi/3, \pi/4$. The end point $\theta = 0$ (not shown) is the zero-flux (in all three planes) Abelian point with $S\tilde{U}(2)$ symmetry in the rotated basis in Fig. 1(b). At $\theta_c = \pi/3$, the WFS with $N_3 = 1$ hits the one with $N_3 = -1$ at the two Fermi points at $\vec{K}_c = (\pm\pi/2, 0, 0)$. As θ decreases further, it becomes a whole Fermi surface (violet) with a total $N_3 = 1 - 1 = 0$ charge, so it is a topologically trivial FS. The remaining four type-I Weyl fermions stay intact through the TQPT. This should be in a different class of TQPTs than in Fig. 4. The coexistence of the four type-I Weyl fermions and the TQPT of the WFS is one of the unique features along this line. The hole WFS can be reached by shifting the particle WFS by one of the two FS nesting vectors, $(0, \pi, \pi), (\pi, \pi, \pi)$.

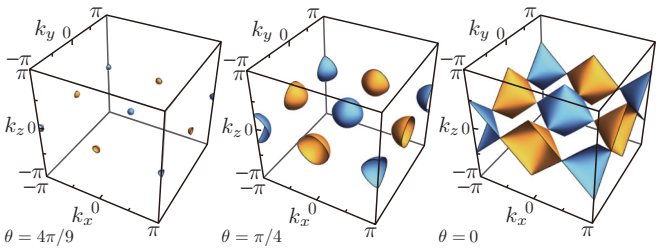

FIG. 6. The particle WFS evolves along $\alpha = \beta = \pi/2, \gamma = \theta$ for $\theta = 4\pi/9, \pi/4, 0$. The TQPT happens at the end point $\theta_c = 0$, where it becomes a corner-sharing octahedron. The hole WFS can be reached by shifting the particle WFS by one of the four FS nesting vectors, $(0, 0, \pi), (\pi, 0, \pi), (0, \pi, \pi), (\pi, \pi, \pi)$. There are also eight straight type-II Weyl fermions at $\theta_c = 0$ shown in Fig. 3.

where $\Delta = \sqrt{3}(\theta_c - \theta)$ is the tuning parameter and $a = 1/2, b = 3/4 + \Delta/4$.

The DOS takes the piecewise form:

$$D(\omega) = \begin{cases} B\left[\Lambda - \sqrt{\frac{-(\omega+\Delta)}{a}}\right], & \omega + \Delta < 0, \\ B\Lambda, & \omega + \Delta > 0, \end{cases} \tag{4}$$

where Λ is the momentum cutoff and $B = \frac{1}{(2\pi)^2 b}$. Note the nonanalytic depletion in the DOS due to the TQPT.

From the DOS, we can evaluate the ground-state energy and find

$$E \sim \begin{cases} \alpha\Delta^2 + \frac{1}{(2\pi)^2 b}\frac{2}{\sqrt{a}}\frac{2}{15}|\Delta|^{5/2} + \cdots, & \Delta < 0, \\ \alpha\Delta^2 + B_0\Delta^3 + \cdots, & \Delta > 0, \end{cases} \tag{5}$$

where $\cdots$ means analytical terms or higher-order nonanalytic terms and α and B_0 are cutoff dependent. Only the leading nonanalytic term is cutoff independent and universal. It is the Δ dependence of b which leads to the background numerical value -0.77.

At half filling $\mu = 0$, plugging the parameters $\Delta = \sqrt{3}(\theta_c - \theta), a = 1/2, b = 3/4 + \Delta/4$ into Eq. (5) and taking two derivatives lead to

$$E''(\theta, \mu = 0) \sim \begin{cases} \alpha + A_0\sqrt{\theta - \theta_c}, & \theta > \theta_c, \\ \alpha + B_0(\theta - \theta_c), & \theta < \theta_c, \end{cases} \tag{6}$$

where the exponents $\nu_- = 1/2, \nu_+ = 1$ are universal and the coefficient $A_0 = 0.18856$ is cutoff independent and stands for the universal contributions from a single cone of the TQPT in Fig. 7. However, B_0 is not universal and cutoff dependent.

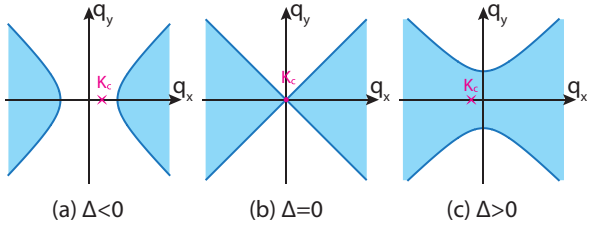

FIG. 7. The FS geometry near the TQPT driven by the particle-particle WFS collision at $K_c = \pi - \theta_c, \theta_c = \pi/3$ in the $q_z = 0$ cross section. $K = \pi - \theta = K_c + \Delta/\sqrt{3}$ is the VHS. The hole-hole WFS collision is similar after changing the shaded regime to a vacuum.

At half filling $\mu = 0$, there are six particle and six hole WFSs colliding at the same time. So in the second derivatives of the total ground-state energy $A = 12A_0 = 2.262$.

We performed numerical calculations on the ground-state energy in the Brillouin zone (BZ) as shown in Appendix A:

$$E_n''(\theta,\mu=0) \sim \begin{cases} -0.77 + A_n(\theta-\theta_c)^{\nu_+}, & \theta > \theta_c, \\ -0.77 + B_n(\theta-\theta_c)^{\nu_-}, & \theta < \theta_c, \end{cases} \quad (7)$$

where subscript n stands for numerical results, the numerical exponents $\nu_+ = 0.5 \pm 0.05, \nu_- = 1.0 \pm 0.05$ match the analytical values $\nu_+ = 1/2, \nu_- = 1$ well and the numerical coefficient $A_n = 2.19$ is also very close to the analytical value $A = 2.262$ achieved above.

IV. SUBLEADING SCALING FUNCTIONS ACROSS THE THIRD TQPT AT FINITE T

It was established [1,2] that near a quantum phase transition at zero temperature, the experimental measurable physical quantities such as single-article Green's functions, specific heat, compressibility, magnetic susceptibilities, etc., should satisfy scaling functions. However, there are always low-energy excitations around the WFS on both sides of the TQPT in Fig. 7. It becomes problematic to apply the scaling analysis near a quantum phase transition with an order parameter to such a TQPT. Unfortunately, the previous RG analysis [12,13] designed to deal with leading scalings around an extended FS do not apply here due to the cone singularity of the FS geometry in Fig. 7. From Eq. (3), intuitively, one can still define the dynamic exponent $z = 2$ with respect to the cone singularity. However, its physical meaning should be quite different from that defined in the QPT with an order parameter and symmetry breaking [1,2] and need to be carefully examined. Indeed, we show that although the leading terms in all these physical quantities are cutoff dependent and nonuniversal, the subleading terms do satisfy universal scaling with $z = 2$, which leads to nonanalytic and therefore non-Fermi-liquid corrections to the leading analytic terms. They always take the sign opposite to the leading term and therefore can be called topological depletions.

Because $z = 2$, one can apply the scaling analysis in [10] here to write down the subleading scaling function for the specific heat and the uniform compressibility $\kappa_u = \chi^{00}(\vec{q} \to 0, \omega = 0)$ for a single particle-particle (or hole-hole) cone in Fig. 7:

$$C_v = \frac{\pi^2}{3} B k_B (k_B T)\Lambda - \frac{B k_B (k_B T)^{3/2}}{\sqrt{a}} \Psi_i\left(\frac{|\Delta|}{k_B T}\right),$$
$$\kappa_u = \frac{1}{2} B\Lambda - \frac{B(k_B T)^{1/2}}{\sqrt{a}} \Omega_i\left(\frac{|\Delta|}{k_B T}\right), \quad (8)$$

where $i = 1,2$ stands for the two sides of the transitions, $\Delta < 0$ and $\Delta > 0$, in Figs. 7 and 8.

Note the first term is the leading term, proportional to the frequency (or energy) cutoff Λ and nonuniversal, while the second term is the subleading term, independent of the frequency (or energy) cutoff Λ and a universal function of the scaling variable $s = \frac{|\Delta|}{k_B T}$. Due to the opposite signs between the two terms, the universal subleading term can be interpreted as the topological depletion coming from the TQPT.

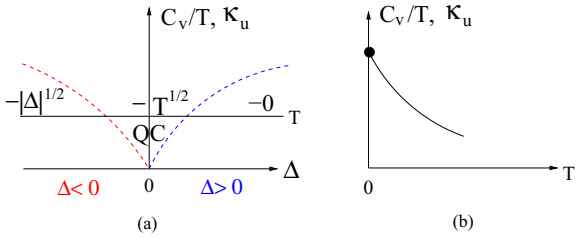

FIG. 8. Experimental signatures of the topological depletions and subleading scalings. (a) The specific heat C_v/T and the compressibility κ_u at a given T show a nonanalytic $\sqrt{T}$ depletion in the QC regime. The FS geometries in the three regimes are shown in Fig. 7. (b) The quantum $\sqrt{T}$ cusps in C_v/T and κ_u in the QC regime in (a) as T decreases. From the ratio of the coefficients of $\sqrt{T}$ in the two quantities, one may also measure the universal topological Wilson ratio R_W^{TD}.

The general forms of the two scaling functions $\Psi_i(x)$ and $\Omega_i(x)$ are evaluated in Appendix B. Here, we list only the topological depletions in the three limiting regimes in Fig. 8 for the specific heat

$$C_v^{TD} = \begin{cases} -\frac{\pi^2}{3}\frac{B}{\sqrt{a}} k_B^2 T\sqrt{|\Delta|}, & \Delta \ll -k_B T, \\ -2.88201\frac{B}{\sqrt{a}} k_B^{5/2} T^{3/2}, & |\Delta| \ll k_B T, \\ -\frac{\sqrt{\pi}}{2}\frac{B k_B^{1/2}}{\sqrt{a}}\frac{\Delta^2}{\sqrt{T}} e^{-\frac{\Delta}{k_B T}}, & \Delta \gg k_B T, \end{cases} \quad (9)$$

and for the uniform compressibility,

$$\kappa_u^{TD} = \begin{cases} -\frac{B}{\sqrt{a}}\sqrt{|\Delta|}, & \Delta \ll -k_B T, \\ -0.536077\frac{B k_B^{1/2} T^{1/2}}{\sqrt{a}}, & |\Delta| \ll k_B T, \\ -\frac{\sqrt{\pi}}{2}\frac{B k_B^{1/2} T^{1/2}}{\sqrt{a}} e^{-\frac{\Delta}{k_B T}}, & \Delta \gg k_B T. \end{cases} \quad (10)$$

One can see both topological depletions are nonanalytic only in the quantum critical (QC) regime in Fig. 8. However, essentially no depletion occurs when $\Delta \gg T$, and a constant $\sqrt{|\Delta|}$ depletion occurs when $-\Delta \gg T$, which can be absorbed by the leading FL contribution anyway. This fact makes their experimental detections feasible (see Sec. VII).

One can also form the topological Wilson ratio $R_W^{TD}(\frac{|\Delta|}{k_B T}) = \frac{k_B^2 T \kappa_u^{TD}}{C_v^{TD}}$, whose values in the three regimes are

$$R_W^{TD} = \begin{cases} 3/\pi^2, & \Delta \ll -k_B T, \\ 0.186, & |\Delta| \ll k_B T, \\ \left(\frac{k_B T}{\Delta}\right)^2, & \Delta \gg k_B T, \end{cases} \quad (11)$$

which is even independent of a and b characterizing the shape of the cone in Fig. 8. In fact, it is also independent of the number of cones participating in the TQPT [14], so it is universal for all the TQPTs in Figs. 4, 5, and 6.

As shown in Appendix B, due to the $[C_4 \times C_4]_D$ symmetry at $\alpha = \beta = \gamma$, the topological depletions of the magnetic susceptibility $\chi^{xx}(T) = \chi^{yy}(T) = \chi^{zz}(T) = \frac{1}{3}\chi^{00}(T)$ also satisfy the subleading scaling equation (10).

V. THE THIRD-ORDER TQPT ALONG THE LINE $\alpha = \pi/2, \beta = \gamma = \theta$ AND THE COEXISTENCE OF FOUR TYPE-I WEYL FERMIONS

At half filling $\mu = 0$, two particle WFSs and two hole WFSs collide at the same time at $\vec{K}_c = (\pi/2,0,0)$ and $\theta_c = \pi/3$. The dispersion near $K_c = \pm\pi/2, \theta_c = \pi/3$ can also be written as Eq. (3), where $\Delta = \sqrt{3}(\theta_c - \theta), a = 1/2, b = 5/8 - \Delta^2/8$. Using Eq. (6), we find $A_0 = 0.2263$; then the two particle WFSs and two hole WFSs contribute to $A = 4A_0 = 0.90$. Similarly, the subleading scaling functions in Eqs. (9) and (10) need also to be multiplied by 4, but the topological Wilson ratio (11) remains identical. As shown in Appendix B, due to the nonconservation of the spins, only the sum over the spin components $\sum_i \chi^{ii}(T) = \kappa_u$ in the magnetic susceptibilities satisfies the subleading scaling equation (10).

We also performed numerical calculation in the whole BZ:

$$E_n''(\theta, \mu = 0) \sim \begin{cases} -0.224 + A_n(\theta - \theta_c)^{\nu_+}, & \theta > \theta_c, \\ -0.224 + B_n(\theta - \theta_c)^{\nu_-}, & \theta < \theta_c, \end{cases} \quad (12)$$

where $A_n = 0.861$ is quite close to the analytic value $A = 4A_0 = 0.90$.

Coexistence of four type-I Weyl fermions

As shown in Fig. 5, there are also four type-I Weyl fermions located at $(0,0,\pi)$, $(0,\pi,0)$, $(\pi,0,\pi)$, $(\pi,\pi,0)$, with the anisotropic dispersion $\epsilon_{\pm}^{I} = -[\frac{1}{2}(q_z^2 - q_y^2) \mp \sqrt{q_x^2 + \sin^2\theta(q_y^2 + q_z^2)}]$. They remain intact through the TQPT, so they just act as four spectators. From the simple scaling analysis with $z = 1$, their contributions to the specific heat are $C_v \sim T^{d/z} \sim T^3$, which is analytic and subleading to the topological analytic depletion $C_v \sim T^{d/z} \sim T^{3/2}$ in the QC regime due to the third-order TQPT. Furthermore, it cannot be distinguished from the analytic T^3 FL corrections. However, they do contribute to the surface Fermi arcs and associated chiral anomalies in the transport properties. How the TQPTs in the bulk in Fig. 5 interfere with the surface Fermi arcs needs to be investigated in a separate publication.

VI. THE FIFTH-ORDER TQPT ALONG THE LINE $\alpha = \beta = \pi/2, \gamma = \theta$ AND THE EIGHT TYPE-II WEYL FERMIONS

How the FS evolves along this line is shown in Fig. 6. As shown in Fig. 6, there is a TQPT at the π flux (in the XY plane) Abelian ending point $\theta_c = 0$ with $S\tilde{U}(2)$ symmetry in the rotated basis in Fig. 1(b). At half filling $\mu = 0$, all four particle WFSs and four hole WFSs collide at the same time at $\theta_c = 0$. Near $\vec{K}_c = (\pi/2,0,0), \theta_c = 0$, the dispersion can also be written as Eq. (3), where $\Delta = -\theta^2/2, a = 1/2, b = 1/2 + \Delta/2$. Note the quadratic dependence of Δ on the SOC tuning parameter θ. Plugging these parameters into Eq. (5), we find

$$E \sim \frac{1}{15\pi^2}|\theta|^5 + \cdots, \quad (13)$$

where $\cdots$ indicates leading analytical terms. Taking five derivatives to get rid of the leading analytic terms leads to

$$\frac{d^5 E}{d\theta^5} \sim \frac{8}{\pi^2}\mathrm{sgn}\theta. \quad (14)$$

It shows that the transition is a fifth-order one. Because all four particle WFSs and four hole WFSs collide at the same time, $A = 8A_0 = \frac{64}{\pi^2}$. Similarly, the subleading scaling functions in Eqs. (9) and (10) also need to be multiplied by 8, but the topological Wilson ratio (11) remains the same.

Type-II Weyl fermions at $\alpha = \beta = \pi/2, \theta = 0$ as a TQPT

One new feature at the TQPT $\theta_c = 0$ is that in addition to the particle-particle and hole-hole WFS collisions, the particle WFS also touches the hole WFS shown in Figs. 6 and 3; such a cone structure between the particle WFS and the hole WFS is nothing but a special case of the type-II Weyl fermions discussed in [15]. Shown in Fig. 3 is essentially a three-dimensional (3D) version of two-dimensional (2D) Dirac fermions. In the 2D case, it is known [16] that there are four Dirac fermions at $\alpha = \beta = \pi/2$ with topological charges $1,-1,1,-1$ at the four time-reversal-invariant momenta $(0,0),(\pi,0),(\pi,\pi),(0,\pi)$. Now adding the third dimension without putting any SOC along it will change the four Dirac fermions into the eight type-II Weyl fermions at the eight momenta, $(0,0,\pm\pi/2),(\pi,0,\pm\pi/2),(\pi,\pi,\pm\pi/2),(0,\pi,\pm\pi/2)$, shown in Fig. 6. Their topological charges are determined by the projections onto the (k_x,k_y) plane, independent of the k_z component and so are still given by $1,-1,1,-1$ at the four projections on the (k_x,k_y) plane: $(k_x,k_y) = (0,0),(\pi,0),(\pi,\pi),(0,\pi)$.

Without losing any generality, we look at the type-II Weyl fermion's dispersion at $(0,0,\pi/2)$:

$$\epsilon_{\pm}^{II}(\vec{q}) = -\big[-q_z \mp \sqrt{q_x^2 + q_y^2}\big], \quad (15)$$

where the plus and minus signs corresponds to the particle and hole WFSs shown in Fig. 3. At $\mu = 0$, taking the minus sign leads to the particle WFS $-q_z \geqslant \sqrt{q_x^2 + q_y^2}$, which takes a cone structure near $(0,0,\pi/2)$. Taking a plus sign leads to the hole WFS $q_z \geqslant \sqrt{q_x^2 + q_y^2}$, which also takes a cone structure above the particle cone shown in Fig. 3. Now putting the SOC $\gamma = \theta$ along the third direction, any small θ immediately opens a gap to both the particle WFS $-q_z \geqslant \sqrt{\theta^2 + q_x^2 + q_y^2}$ near $(0,0,0)$ and the hole WFS $q_z \geqslant \sqrt{\theta^2 + q_x^2 + q_y^2}$ near $(0,0,\pi)$ with the dynamic exponent $z = 1$ in Fig. 3. At the same time, the four particle WFSs split with the form (3) with the dynamic exponent $z = 2$. The four hole WFSs also split at the four FS nesting momenta. When θ gets close to $\pi/2$, the particle and the hole WFSs shrink to a small sphere with $q_x^2 + q_y^2 + q_z^2 = (\pi/2 - \theta)^2$ shown in Fig. 2. At $\theta = \pi/2$, they shrink to the type-I Weyl fermion shown in Fig. 1. Although a type-I fermion is a semimetal, in the type-II Weyl fermion, both the extended particle and hole WFSs add together to contribute to a finite DOS $D(\omega) \sim \Lambda^2 - \alpha\omega^2$ with a possible topological depletion in DOS of $\sim\alpha\omega^2$, so it is a metallic phase [17]. For tilted type-II Weyl fermions in [15], $\alpha > 0$. However, for the special straight type-II Weyl fermions in Fig. 3, $\alpha = 0$.

From the simple scaling analysis, the eight type-II Weyl fermions with $z = 1$ contribute to the specific heat $C_v^D \sim \alpha T^3$, which is subleading to the topological depletion $C_v^D \sim T^{3/2}$ due to the fifth-order TQPT in the QC regime. In fact, as stated above, for the straight type-II Weyl fermions, even the coefficient $\alpha = 0$, so it does not even have a topological depletion to C_v^D, χ_u^D.

VII. EXPERIMENTAL REALIZATIONS AND DETECTIONS IN COLD ATOMS AND MATERIALS

The Hamiltonian (1) of free fermions hopping in a cubic lattice subject to a Weyl type of spin-orbit coupling can be achieved by loading cold atoms in a cubic optical lattice. Indeed, recently, 2D SOC was experimentally implemented in the fermion ^{40}K gas [18,19]. Soon after, using an optical Raman lattice scheme, the authors of the experiment in [20] realized the Rashba SOC of spinor bosons with tunable (α, β) in a square lattice. An optical lattice clock scheme [21] was proposed to generate a 2D SOC in an optical lattice; it has the advantage of suppressing the possible heating issue. Most recently, by using the most magnetic fermionic element, dysprosium, to eliminate the heating due to the spontaneous emission, the authors in [22] created a long-lived SOC gas of quantum degenerate atoms. The long lifetime of this weakly interacting SOC degenerate Fermi gas will facilitate the experimental study of quantum many-body phenomena that manifest at longer time scales. The heating issues with fermions may be more serious than those with spinor bosons. However, the TQPTs in Figs. 4, 5, and 6 are for noninteracting fermions; they are essentially single-particle properties, so the heating issues should be manageable in current cold-atom experiments with fermions.

Of course, all experiments are performed at finite temperatures which are controlled by the topological phase transitions at $T = 0$ in Figs. 4, 5, and 6. The TQPTs do not survive at finite $T > 0$ but become the three crossover regimes shown in Fig. 8. The crossover temperature can be estimated as $T \sim \Delta \sim t \sim 3$ nK, which is easily experimentally reachable with the current cooling techniques [23,24], so the $\sqrt{T}$ quantum cusp behaviors in $C_v/T, \kappa_u$, and the universal topological Wilson ratio in Fig. 8, could be detected by the specific-heat measurements [25,26], *in situ* measurements [27], and the compressibility κ measurements [26]. The change in the FS topology across the TQPTs in Figs. 4, 5, and 6 and in the type-I Weyl fermions in Fig. 2 and type-II Weyl fermions in Fig. 3 can be monitored by the momentum-resolved interband transitions [28] and the band-mapping technique developed in [20].

As shown in Figs. 4, 5, and 6, type-I fermions are quite common and robust in this simple SOC model. However, the type-II fermions seem quite restricted; also only straight type-II fermions different from the tilted type-II proposed in [15] can be realized. Subleading scaling functions in Eqs. (9) and (10) can be easily extended to the type-II Weyl fermions with $z = 1$ in these materials. Unfortunately, the topological depletion $\sim T^3$ is analytic and cannot be distinguished from the FL corrections, which are also T^3. As noted above, there is no such topological depletion for the straight type-II fermions. Type-I Weyl fermions have been discovered in several materials [29–33]. Type-II Weyl fermions [15] also seem to have been found in a few materials, although there are still quite controversial experimental interpretations on the number of bulk type-II Weyl fermions and associated surface Fermi arcs [34,35]. Topological Lifshitz transitions happen in all these type-I and type-II Weyl fermion materials. Although they may not be described precisely by the Hamiltonian (1), they should be in the same topological classes as those in Figs. 4, 5, and 6. So the results achieved in this paper should also apply to the topological Lifshitz transitions in these noninteracting or weakly interacting materials.

VIII. DISCUSSIONS AND CONCLUSIONS

We may classify the FS topologies at half filling in terms of topological phase transitions and associated leading or subleading scaling functions. There are two kinds of TQPTs: (1) the first one is between a particle and a hole, which leads to type-I and type-II fermions. (a) Type-I Weyl fermions are relativistic, have closed particle or hole FSs with the DOS $D(\omega) \sim \omega^2$, and satisfy leading analytic scaling with the dynamic exponent $z = 1$. (b) Type-II Weyl fermions are nonrelativistic, have extended open particle and hole FSs with the DOS $D(\omega) \sim \Lambda^2 - \alpha\omega^2$, and satisfy subleading analytic scaling with the dynamic exponent $z = 1$. (2) The second one is the TQPT between a particle and another particle (or a hole and another hole) through a cone singularity, has extended FSs on both sides with the DOS given in Eq. (4), and satisfy subleading nonanalytic scaling with the dynamic exponent $z = 2$. Our preliminary results away from half filling show there are new classes of TQPT with anisotropic dynamic exponents [36]. Of course, at sufficiently large μ, there is a quadratic band touching through a closed hole FS with the DOS $D(\omega) \sim \sqrt{\omega}, \omega > 0, D(\omega) = 0, \omega < 0$. It leads a metal to Band insulator (BI) transition which satisfies a leading nonanalytic scaling with dynamic exponent $z = 2$. The results will be presented in a future publication. It would also be interesting to look at the physical classification here from formal K-theory classification. However, so far, the K-theory classification assumes only the translational symmetry and ignores the constraints from crystalline symmetries which take the spin-orbital-coupled crystalline symmetries in Eq. (1).

Equations (9) and (10) take a form similar to the topological entanglement entropy [37]: $S = \alpha L - \gamma$, where the first term is the leading nonuniversal term proportional to the length between the boundary of the two entangled regimes, A and B. The second term is the subleading term, independent of the boundary and universal, called the topological entanglement entropy $\gamma = \ln D$, where D is the quantum dimension (which is a counterpart of the dynamic exponent z here). There is also a relative minus sign between the two terms. This suggests that the form may be a general scaling structure across a TQPT, in sharp contrast to the conventional leading scaling across a conventional QPT with an order parameter and associated symmetry breaking.

The subleading scaling behaviors in the specific heat in Eq. (9) resemble the specific heat near the finite-temperature

phase transition of the classical $O(3)$ Heisenberg model [38] $C_v \sim C - b_0 t^{-\alpha}$, where $t = |(T - T_c)/T_c|, b_0 > 0$, and $\alpha \sim -0.1$. So the specific heat will show a maximum classical cusp near T_c. This cusp has been precisely detected in specific-heat experiments. This fact has also been used to determine the anomalous Hall effect near the finite-temperature phase transition in [39]. Here, the quantum $\sqrt{T}$ cusp behavior in the QC regime near $T = 0$ in Fig. 8 is due to the TQPT at $(T = 0, \Delta = 0)$. So the mechanism of the quantum cusp discovered in this paper is completely different than that of the classical cusp.

As shown in Figs. 4, 5, and 6, type-I fermions are quite common in this simple model, in contrast to the Weyl semimetals in materials [29–33] which have only two (or four) Weyl points if the time-reversal (or inversion) symmetry is broken. Here, there are eight and four Weyl points in Figs. 1(c) and 5, respectively, due to the inversion symmetry breaking. The present paper focused on the TQPTs in the bulk. Taking a slab geometry with two surfaces (in real space) parallel to the $(1,1,1)$ direction, every Fermi arc connects one $+1$ to one -1 monopole, so it may be interesting to investigate how the Fermi arcs in the two surfaces connect the projections of the eight or four Weyl points onto the two surfaces and monitor how the Fermi arcs reconstruct across the TQPT in the bulk in Figs. 4 and 5. While eight type-II fermions seem quite restrictive, they are realized only at the π flux in Abelian point $\alpha = \beta = \pi/2, \gamma = 0$ in Fig. 6. It remains unknown if there is a well-defined surface Fermi arc associated with these eight straight type-II fermions.

In terms of scaling functions, the TQPT in Figs. 4, 5, and 6 should all be in the same universality class. The topological Wilson ratio is even identical. However, the main difference is that the WFS is still topologically nontrivial, carrying a topological charge $N_3 = -2$ after the TQPT in Fig. 4, but becomes trivial in Figs. 5 and 6. It seems the scaling functions near a single cone may not reflect the total topological charges carried by the WFS. Different TQPTs may be described by the same set of scaling functions. However, the total coefficient A does depend on the global topology of the WFS which is related to N_3.

Due to the vanishing of the DOS at the type-I Weyl point, a weak interaction is irrelevant. But due to the extended FS at the type-II Weyl point and the particle-particle or hole-hole TQPT point, any weak interaction is relevant. Following Refs. [16,40–42], it is important to look at the effects of both positive U and negative U. For example, $U > 0$ and away from half filling, due to $N_3 = -2$ in Fig. 4, depending on the signs of the pairing amplitudes in different parts of WFS, it may lead to new time reversal (TR) invariant topological superfluids with an associated Majorana surface mode [7].

ACKNOWLEDGMENTS

We thank Yu Yi-Xiang for early participation in the Project and acknowledge AFOSR Grant No. FA9550-16-1-0412 for the support. The work at KITP was supported by NSF Grant No. PHY11-25915.

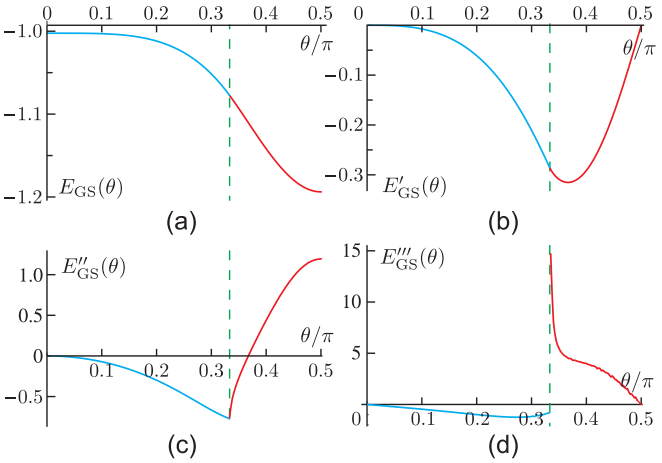

FIG. 9. The ground-state energy density and its derivatives on the lattice versus the SOC parameter θ/π. (a) The ground-state energy. (b) Its first-order derivative. (c) Its second-order derivative. (d) Its third-order derivative. So the TPT at $\theta_c = \pi/3$ is a third-order one.

APPENDIX A: NUMERICAL EVALUATION OF ZERO-TEMPERATURE UNIVERSAL AMPLITUDE AND CRITICAL EXPONENTS IN THE TQPTS

The ground-state energy along the line $\alpha = \beta = \gamma = \theta$ is calculated as

$$E_{\rm GS}(\theta) = \frac{1}{(2\pi)^3} \int_{\rm kfilled} d\mathbf{k}[\epsilon_+(\mathbf{k};\theta) + \epsilon_-(\mathbf{k};\theta)], \tag{A1}$$

whose numerical results are given in Fig. 9.

It is obvious that when $\theta < \theta_c$, $E''(\theta) \sim (\theta - \theta_c)$. But when $\theta > \theta_c$, it should be $E''(\theta) \sim (\theta - \theta_c)^{\nu_+}$ with some value $\nu_+ < 1$. The best fits leads to Eq. (7) with the coefficient $A_n = 2.19$ and the critical exponent $\nu_+ = -(0.50 \pm 0.05)$, which matches the analytic values well.

We also performed similar calculations along the other two lines, $\alpha = \pi/2, \beta = \gamma = \theta$ and $\alpha = \beta = \pi/2, \gamma = \theta$, and also found the numerical values match the analytic ones precisely.

APPENDIX B: EVALUATIONS OF FINITE-TEMPERATURE UNIVERSAL SUBLEADING SCALING FUNCTIONS ACROSS A TQPT

The internal energy is

$$U = \int_{-\infty}^{\infty} d\omega \frac{D(\omega)\omega}{e^{\frac{\omega}{k_B T}} + 1}, \tag{B1}$$

which leads to the specific heat:

$$C_v = \frac{\partial U}{\partial T} = k_B \int_{-\infty}^{\infty} d\omega D(\omega) \frac{e^{\frac{\omega}{k_B T}}}{(e^{\frac{\omega}{k_B T}} + 1)^2} \frac{\omega^2}{(k_B T)^2}. \tag{B2}$$

Plugging in the DOS in Eq. (3) leads to the first equation in the scaling form equation (7) with the scaling variable $s = \frac{|\Delta|}{k_B T}$, where

$$\Psi_1(s) = \int_0^s dx \frac{\sqrt{s-x}x^2 e^x}{(e^x+1)^2} + \int_0^\infty dx \frac{\sqrt{s+x}x^2 e^x}{(e^x+1)^2},$$
$$\Psi_2(s) = \int_s^\infty dx \frac{\sqrt{x-s}x^2 e^x}{(e^x+1)^2}. \tag{B3}$$

However, the compressibility and magnetic susceptibility involve the Hamiltonian, not just the DOS. From Eq. (1), one can get the fermion Green's function:

$$G(i\omega,k) = [i\omega - H_k]^{-1} = \sum_{s=\pm} \frac{P_s(k)}{i\omega - \epsilon_s(k)}, \tag{B4}$$

where $P_s = \frac{1}{2}[\sigma_0 + s\sum_i \frac{h_i}{h}\sigma_i]$ are the projection operators onto the particle-hole bands $s = \pm$.

The dynamic density-spin susceptibility is

$$\chi^{\mu\nu}(q,i\omega_n) = -k_B T \sum_{k,iv} \mathrm{Tr}[G(i\omega_n + iv_n,k')\sigma^\mu G(iv_n,k)\sigma^\nu], \tag{B5}$$

where $k' = k + q$.

Working out the sum over the Matsubara frequency leads to

$$\chi^{\mu\nu}(q,i\omega_n) = -\sum_{k,s,s'} M^{\mu\nu}_{ss'}(k,k') \frac{f_{sk} - f_{s'k'}}{i\omega_n - \epsilon^{s'}_{k'} + \epsilon^{s}_{k}}, \tag{B6}$$

where the Fermi distribution function $f_{sk} = f(\epsilon^s_k)$ and $M^{\mu\nu}_{ss'}(k,k') = \mathrm{Tr}[P_s(k)\sigma^\mu P_{s'}(k')\sigma^\nu]$.

In the static limit, we have

$$\lim_{q\to 0} \frac{f_{sk} - f_{s'k'}}{\epsilon^s_k - \epsilon^{s'}_{k+q}} = \delta_{ss'}\frac{\partial f(\epsilon)}{\partial \epsilon} + \delta_{s,-s'}\frac{f_{sk} - f_{s'k}}{2sh(k)} \tag{B7}$$

and $\lim_{q\to 0} M^{\mu\nu}_{ss'}(k,k') = M^{\mu\nu}_{ss}(k,k)\delta_{ss'}$, which is evaluated as

$$M^{\mu\nu}_{ss}(k,k) = \begin{pmatrix} 1 & s\frac{h_x}{h} & s\frac{h_y}{h} & s\frac{h_z}{h} \\ s\frac{h_x}{h} & \frac{h_x^2}{h^2} & \frac{h_x h_y}{h^2} & \frac{h_x h_z}{h^2} \\ s\frac{h_y}{h} & \frac{h_x h_y}{h^2} & \frac{h_y^2}{h^2} & \frac{h_y h_z}{h^2} \\ s\frac{h_z}{h} & \frac{h_x h_z}{h^2} & \frac{h_y h_z}{h^2} & \frac{h_z^2}{h^2} \end{pmatrix}. \tag{B8}$$

Because the particle and hole WFSs collide at momenta differing by $\vec{Q} = (\pi,\pi,\pi)$, in extracting nonanalytic contributions, one can drop the mixing between particle and hole WFSs and focus on just one collision cone between the particle-particle or hole-hole WFS. Then a single cone compressibility is

$$\kappa_u(T) = \chi^{00}(T) = -\int_{-\infty}^{+\infty} d\omega D(\omega)\frac{\partial}{\partial\omega}\frac{1}{e^{\frac{\omega}{k_B T}} + 1}. \tag{B9}$$

Plugging in the DOS in Eq. (3) leads to the second equation in the subleading scaling form equation (7), where

$$\Omega_1(s) = \int_0^s dx \frac{\sqrt{s-x}e^x}{(e^x+1)^2} + \int_0^\infty dx \frac{\sqrt{s+x}e^x}{(e^x+1)^2},$$
$$\Omega_2(s) = \int_s^\infty dx \frac{\sqrt{x-s}e^x}{(e^x+1)^2}. \tag{B10}$$

From Eq. (B8), one can also read the single-cone spin susceptibility:

$$\chi^{ij}(T) = -\int d^3k \frac{h_i h_j}{h^2}\frac{\partial}{\partial\omega}\frac{1}{e^{\frac{\omega}{k_B T}} + 1}\bigg|_{\omega=\omega_s(k)}, \tag{B11}$$

where $i,j = x,y,z$.

Since h_i is an odd function of k, we have $\chi^{ij}(T) = \delta_{ij}\chi^{ii}(T)$. Using the identity $h^2 = h_x^2 + h_y^2 + h_z^2$, we get the following sum rule for the subleading scaling which holds for any (α,β,γ):

$$\sum_i \chi^{ii}(T) = \kappa_u. \tag{B12}$$

Indeed, like in the theoretical evaluations and experimental detections of the coherence length in a SOC system [43], because the spin is not conserved, we expect only that the average over all the spin components satisfies the subleading scalings.

However, the enlarged $[C_4 \times C_4]_D$ symmetry at $\alpha = \beta = \gamma = \theta$ dictates

$$\chi^{xx}(T) = \chi^{yy}(T) = \chi^{zz}(T) = \tfrac{1}{3}\chi^{00}(T), \tag{B13}$$

which also satisfies the subleading scaling individually.

[1] S. Sachdev and J. Ye, Universal Quantum-Critical Dynamics of Two-Dimensional Antiferromagnets, Phys. Rev. Lett. **69**, 2411 (1992); A. V. Chubukov, S. Sachdev, and J. Ye, Theory of two-dimensional quantum Heisenberg antiferromagnets with a nearly critical ground state, Phys. Rev. B **49**, 11919 (1994).

[2] S. Sachdev, *Quantum Phase Transitions*, 2nd ed. (Cambridge University Press, Cambridge, 2011).

[3] X. G. Wen and Q. Niu, Phys. Rev. B **41**, 9377 (1990); X. G. Wen, *Quantum Field Theory of Many-Body Systems* (Oxford University Press, Oxford, 2004).

[4] G. E. Volovik, *The Universe in a Helium Droplet* (Oxford University Press, New York, 2003).

[5] G. E. Volovik, Exotic Lifshitz transitions in topological materials, arXiv:1701.06435; Topological Lifshitz transitions, Low Temp. Phys. **43**, 47 (2017); K. Zhang and G. E. Volovik, Lifshitz transitions, type-II Dirac and Weyl fermions, event horizon and all that, arXiv:1604.00849. Note that these preprints focus on the topological invariants across various topological phase transitions and so are complementary to the present work.

[6] M. Z. Hasan and C. L. Kane, Colloquium: Topological insulators, Rev. Mod. Phys. **82**, 3045 (2010).

[7] X. L. Qi and S. C. Zhang, Topological insulators and superconductors, Rev. Mod. Phys. **83**, 1057 (2011).

[8] J. Ye and S. Sachdev, The Effects of Coulomb Interaction on Quantum Hall Critical Points of Systems in a Periodic Potential, Phys. Rev. Lett. **80**, 5409 (1998).

[9] J. Ye, The effects of weak disorders and Coulomb interaction on quantum Hall critical points, Phys. Rev. B **60**, 8290 (1999).

[10] F. Sun, X.-L. Yu, J. Ye, H. Fan, and W. M. Liu, Topological quantum phase transition in synthetic non-Abelian gauge potential: Gauge invariance and experimental detections, Sci. Rep. **3**, 2119 (2013).

[11] S.-S. Zhang, J. Ye, and W.-M. Liu, Itinerant magnetic phases and quantum Lifshitz transitions in repulsively interacting spin-orbit coupled Fermi gas, Phys. Rev. B **94**, 115121 (2016).

[12] R. Shankar, Renormalization-group approach to interacting fermions, Rev. Mod. Phys. **66**, 129 (1994).

[13] J. Ye and S. Sachdev, Superconducting, metallic, and insulating phases in a model of CuO_2 layers, Phys. Rev. B **44**, 10173 (1991).

[14] In fact, the Wilson ratio $R_w = (\frac{k_B T}{\Delta})^2$ in the $\Delta \gg k_B T$ regime here is identical not only to that in a 2D TQPT driven by the collisions of Dirac fermions in a honeycomb lattice in [10] but also to that in the rotated ferromagnetic Heisenberg model in [42] and rotated antiferromagnetic ferromagnetic Heisenberg model in [16], where the Wilson ratio is defined as the ratio of the conserved magnetic susceptibility over the specific heat. It is not known why it is identical in all these unrelated models.

[15] A. A. Soluyanov, D. Gresch, Z. Wang, Q. Wu, M. Troyer, X. Dai, and B. A. Bernevig, Type-II Weyl Semimetals, Nature (London) **527**, 495 (2015).

[16] F. Sun, J. Ye, and W.-M. Liu, Fermionic Hubbard model with Rashba or Dresselhaus spin-orbit coupling, New J. Phys. **19**, 063025 (2017).

[17] We think that the title "Type-II Weyl Semimetals" in Ref. [15] maybe misleading because type-II Weyl fermions lead to a metal instead of a semimetal.

[18] L. Huang, Z. Meng, P. Wang, P. Peng, S.-L. Zhang, L. Chen, D. Li, Q. Zhou, and J. Zhang, Experimental realization of a two-dimensional synthetic spin-orbit coupling in ultracold Fermi gases, Nat. Phys. **12**, 540 (2016).

[19] Z. Meng, L. Huang, P. Peng, D. Li, L. Chen, Y. Xu, C. Zhang, P. Wang, and J. Zhang, Experimental Observation of a Topological Band Gap Opening in Ultracold Fermi Gases with Two-Dimensional Spin-Orbit Coupling, Phys. Rev. Lett. **117**, 235304 (2016).

[20] Z. Wu, L. Zhang, W. Sun, X.-T. Xu, B.-Z. Wang, S.-C. Ji, Y. Deng, S. Chen, X.-J. Liu, and J.-W. Pan, Realization of two-dimensional spin-orbit coupling for Bose-Einstein condensates, Science **354**, 83 (2016).

[21] M. L. Wall, A. P. Koller, S. Li, X. Zhang, N. R. Cooper, J. Ye, and A. M. Rey, Synthetic Spin-Orbit Coupling in an Optical Lattice Clock, Phys. Rev. Lett. **116**, 035301 (2016).

[22] N. Q. Burdick, Y. Tang, and B. L. Lev, Long-Lived Spin-Orbit-Coupled Degenerate Dipolar Fermi Gas, Phys. Rev. X **6**, 031022 (2016).

[23] P. Medley, D. M. Weld, H. Miyake, D. E. Pritchard, and W. Ketterle, Spin Gradient Demagnetization Cooling of Ultracold Atoms, Phys. Rev. Lett. **106**, 195301 (2011).

[24] S. Sugawa, K. Inaba, S. Taie, R. Yamazaki, M. Yamashita, and Y. Takahashi, Interaction and filling-induced quantum phases of dual Mott insulators of bosons and fermions, Nat. Phys. **7**, 642 (2011).

[25] J. Kinast, A. Turlapov, J. E. Thomas, Q. Chen, J. Stajic, and K. Levin, Heat capacity of a strongly interacting Fermi gas, Science **307**, 1296 (2005).

[26] M. J. H. Ku, A. T. Sommer, L. W. Cheuk, and M. W. Zwierlein, Revealing the superfluid lambda transition in the universal thermodynamics of a unitary Fermi gas, Science **335**, 563 (2012).

[27] N. Gemelke, X. Zhang, C. L. Huang, and C. Chin, In situ observation of incompressible Mott-insulating domains in ultracold atomic gases, Nature (London) **460**, 995 (2009).

[28] L. Tarruell, D. Greif, T. Uehlinger, G. Jotzu, and T. Esslinger, Creating, moving and merging Dirac points with a Fermi gas in a tunable honeycomb lattice, Nature (London) **483**, 302 (2012).

[29] S.-Y. Xu, M. Zahid Hasan *et al.*, Discovery of a Weyl fermion state with Fermi arcs in niobium arsenide, Nat. Phys. **11**, 748 (2015).

[30] S.-Y. Xu, M. Zahid Hasan *et al.*, Discovery of a Weyl fermion semimetal and topological Fermi arcs, Science **349**, 613 (2015).

[31] L. X. Yang, Y. L. Chen *et al.*, Weyl semimetal phase in the non-centrosymmetric compound TaAs, Nat. Phys. **11**, 728 (2015).

[32] B. Q. Lv, H. Ding *et al.*, Observation of Weyl nodes in TaAs, Nat. Phys. **11**, 724 (2015).

[33] L. Lu, Z. Wang, D. Ye, L. Ran, L. Fu, J. D. Joannopoulos, and M. Soljačić, Experimental observation of Weyl points, Science **349**, 622 (2015).

[34] Z. Wang, D. Gresch, A. A. Soluyanov, W. Xie, S. Kushwaha, X. Dai, M. Troyer, R. J. Cava, and B. A. Bernevig, $MoTe_2$: A Type-II Weyl Topological Metal, Phys. Rev. Lett. **117**, 056805 (2016).

[35] A. Tamai, Q. S. Wu, I. Cucchi, F. Y. Bruno, S. Riccò, T. K. Kim, M. Hoesch, C. Barreteau, E. Giannini, C. Besnard, A. A. Soluyanov, and F. Baumberger, Fermi Arcs and Their Topological Character in the Candidate Type-II Weyl Semimetal $MoTe_2$, Phys. Rev. X **6**, 031021 (2016).

[36] The leading anisotropic dynamic exponents associated with the bosonic analog of the type-II Weyl fermions occur in the rotated ferromagnetic Heisenberg model in a longitudinal Zeeman field [40] but not in a transverse field [41].

[37] M. Levin and X. G. Wen, Detecting Topological Order in a Ground State Wave Function, Phys. Rev. Lett. **96**, 110405 (2006); A. Kitaev and J. Preskill, Topological Entanglement Entropy, *ibid.* **96**, 110404 (2006).

[38] C. Holm and W. Janke, Monte Carlo study of topological defects in the 3D Heisenberg model, J. Phys. A **27**, 2553 (1994); M. H. Lau and C. Dasgupta, Numerical investigation of the role of topological defects in the three-dimensional Heisenberg transition, Phys. Rev. B **39**, 7212 (1989); M. Kamal and G. Murthy, New O(3) Transition in three Dimensions, Phys. Rev. Lett. **71**, 1911 (1993).

[39] J. Ye, Y. B. Kim, A. J. Millis, B. I. Shraiman, P. Majumdar, and Z. Tešanović, Berry Phase Theory of the Anomalous Hall Effect: Application to Colossal Magnetoresistance Manganites, Phys. Rev. Lett. **83**, 3737 (1999).

[40] F. Sun, J. Ye, and W.-M. Liu, Quantum incommensurate skyrmion crystal phases and commensurate to in-commensurate transitions of cold atoms and materials with spin orbit couplings, New J. Phys. (to be published), arXiv:1502.05338.

[41] F. Sun, J. Ye, and W.-M. Liu, Classification of magnons in rotated ferromagnetic Heisenberg model and their competing responses in transverse fields, Phys. Rev. B **94**, 024409 (2016).

[42] F. Sun, J. Ye, and W.-M. Liu, Quantum magnetism of spinor bosons in optical lattices with synthetic non-Abelian gauge fields at zero and finite temperatures, Phys. Rev. A **92**, 043609 (2015).

[43] Y.-X. Yu, J. Ye, and W.-M. Liu, Coherent lengths in attractively interacting Fermi gases with spin-orbit couplings, Phys. Rev. A **90**, 053603 (2014).